Hole-vortex-magnons interactions in diluted layered antiferromagnets with planar symmetry

A. R. Pereira*
Departamento de Física, Universidade Federal de Viçosa, Viçosa, 36570-000, Minas Gerais, Brazil

G. M. Wysin†
Department of Physics, Kansas State University, Manhattan, KS 66506-2601
(Dated: April 19, 2006)

We investigate the scattering of spin wave or magnon modes on planar vortices pinned on holes in two-dimensional (2D) easy-plane antiferromagnets. Numerical methods on a discrete lattice and analytical calculations in a continuum model are considered. Numerical calculations use systems centered on a lattice site, whose spin is removed. The continuum treatment is based on a simple approach that solves the equations of motion on a 2D support manifold not simply connected (i.e., containing a circular hole, which can be seen as a spin vacancy). The phase-shifts for the scattered states are obtained and a comparison between numerical and analytical results is discussed. The vortex instability local mode is analyzed as a function of the hole size by several approaches. Its frequency is found to go to zero at a critical hole size. Larger holes are found to be more effective for stabilizing vortices in the planar configuration.

PACS numbers: 75.10.Hk, 75.10.-b, 05.45.Yv

I. INTRODUCTION

In the last years much attention has been given to nonlinear excitations in low dimensional magnetic materials. For instance, vortices develop important roles in the static and dynamic properties of two-dimensional (2D) magnets with easy-plane anisotropy. In particular, the scattering of spin waves by vortices in "pure" 2D easy-plane magnets has been studied both analytically[1,2,3] and numerically[4,5,6,7,8,9], for a variety of uniform magnetic systems in which a single vortex has been placed. Rich structures have been found, including localized modes[4,5,6] associated with the in-plane to out-of-plane vortex transition,[10,11] a connection between low angular momentum vortex-spin wave states and vortex translational motion,[7,12] and fascinating effects induced by a magnetic field perpendicular to the easy plane in ferromagnets.[8] The scattering phase shifts have been investigated numerically and analytically for pure ferromagnets and antiferromagnets, indicating stronger scattering at the lower angular momenta, due to the (low winding number) effective potential of the vortex core.

However, real compounds are not ideal systems and lattice defects such as impurities and local fields are present in any material sample. The effect of impurities on superconductors has been of theoretical and experimental interest even in its own right for a long time. Vortex pinning mechanisms and even antiferromagnetic correlations in the cuprates[13,14] are phenomena related to impurities. Hence, the interaction of topological excitations with spatial inhomogeneities is of considerable importance from both the purely theoretical and applied points of view.

The effect of nonmagnetic impurities (spin vacancies) on vortex excitations has recently been studied for 2D magnetic models. Recent analytical calculations,[15,16,17,18] spin energy relaxation and Monte Carlo simulations,[17,19,20] and even experimental results[21,22] show that nonmagnetic impurities tend to attract and even pin vortices,[16,19,23] and in the process, lower their energy of formation and lower the transition temperature[24,25,26,27] associated with vortex-antivortex pair unbinding.[28,29,30] A missing spin site also lowers the easy-plane anisotropy strength needed for planar vortex stabilization,[23,34] a static property. Such properties have aided Zaspel *et al.*[31,32] to experimentally investigate the pinned vortices in isotropic AFMs using electron paramagnetic resonance. Also, pinned vortices may be seen in easy-plane magnets using neutron scattering experiments.[33]

While various static properties were already considered for these impurity systems, almost nothing is known about the dynamics. A natural further step is the study of the scattering of spin waves by pinned vortices in inhomogeneous magnetic materials, the most basic dynamical property to be understood. Therefore, in this paper we investigate the scattering of spin waves by a vortex that is itself pinned on a nonmagnetic impurity in an easy-plane antiferromagnet (AFM).

We study the vortex–spin wave scattering for planar AFM vortices assuming that the easy-plane anisotropy strength is above the critical value that stabilizes a pinned vortex in the planar form.[23,34] We consider both a continuum model and a discrete lattice model for this problem.[3,35] In the continuum model, it is assumed that there is a small hole of radius r_0 cut from the system center, located at the origin, on which a vortex is pinned. The magnetic degrees of freedom are defined only outside this hole. This model allows for the investigation of scattering effects as a function of the hole radius (the hole radius should also affect the vortex stability and pinning energy.). In the discrete lattice model, using a square

lattice, the finite system is circular, and one lattice site or spin has been removed at its center, where a vortex pins. This latter model allows for the investigation of effects due to individual atomic impurities. We expect to be able to compare these models, to a certain extent, when the hole size is on the order of the lattice constant, $r_0 \approx a$.

It should be interesting to determine how the magnon properties change with the size of the hole. One can expect the critical anisotropy strength to change with the size of the hole, which could have future technological applications. The scattering phase shifts can also be expected to be different, depending on whether a hole has pinned a vortex, or not. Scattering could possibly be used to "read" the presence of a pinned vortex. Also, the scattering properties will change with the charge q of the pinned vortex—the presence of a hole or vacancy has been found to lead to the possibility of stable doubly-charged vortices.[26] Thus, the scattering could be used to distinguish the charge of a pinned vortex.

The paper is organized as follows. First, the continuum model is further described in Sec. II, and then the continuum limit equations for the acoustic and optical spin wave modes of a vortex pinned on a hole are discussed in Sec. III, in terms of the scattering phase shifts expected in the different angular momentum channels. In Sec. IV we give a description of the numerical method used to calculate some of the lowest modes and scattering phase shifts in a finite square-lattice circular system, as well as the associated numerical results. For both the continuum and numerical calculations, modes in which the absolute angular momentum quantum number is less than the absolute vortex charge merit special attention, due to the appearance of Bessel functions of imaginary order. This is followed in Sec. V by a general analysis of the pinned-vortex instability mode (VIM)–a bound state of strong out-of-plane amplitude, localized on the vortex (or hole), and associated with the destabilization towards formation of an out-of-plane vortex. Finally, implications of these results for experiments on magnetic materials with nonmagnetic impurities and/or intentionally placed holes are given in Sec. VI.

II. MODEL

We consider a 2D AFM easy-plane classical spin system, with combined exchange and single ion anisotropy terms λ and d, with Hamiltonian

$$H = J\sum_{i,j}\{\frac{1}{2}[S_i^x S_j^x + S_i^y S_j^y + \lambda S_i^z S_j^z] + d(S_i^z)^2\}, \quad (1)$$

where the sum is over the nearest neighbor sites, $J > 0$ is the exchange constant and $\vec{S}_i = \{S_i^x, S_i^y, S_i^z\}$ is the classical spin vector at site located at $\vec{r}_i$. The square lattice system has lattice constant a. The continuum limit of this Hamiltonian can be obtained defining normalized vectors of magnetization $\vec{m}_n = (\vec{S}_{2n} + \vec{S}_{2n+1})/2S$ and the vectors of sublattice magnetization $\vec{l}_n = (\vec{S}_{2n} - \vec{S}_{2n+1})/2S$, where the subscripts refer to the different sublattices. Vectors $\vec{m}$ and $\vec{l}$ are related by $\vec{m}^2 + \vec{l}^2 = 1$ and $\vec{m} \cdot \vec{l} = 0$. In the limit of low temperatures, the condition $\mid \vec{m} \mid \ll \mid \vec{l} \mid \approx 1$ is satisfied and then the continuum Hamiltonian can be expressed in terms of $\vec{l}$ only. There is a hole cut out centered on the origin, of radius r_0. Then the Hamiltonian can be written as[15] $H_I = \int d^2x \; h(\vec{l}, \partial_\mu \vec{l}) U(\vec{r})$, where $h(\vec{l}, \partial_\mu \vec{l})$ is the Hamiltonian density (given by the anisotropic nonlinear σ model) and $U(\vec{r})$ is a function that represents the hole (the nonmagnetic impurity) centralized at origin, defined as $U(\vec{r}) = 0$ if $\mid \vec{r} \mid < r_0$ and $U(\vec{r}) = 1$ if $\mid \vec{r} \mid \geq r_0$. Above, the covariant derivative is defined as $\partial_\mu = ((1/c)\partial/\partial t, \partial/\partial x, \partial/\partial y)$, where c is the velocity of long-wavelength magnons. A charge q vortex can be assumed to be pinned and centered on the hole; this will be the preferred configuration that minimizes the static energy. The desired spin wave (or magnon) modes will be the small amplitude oscillations around the static spin structure, which is assumed to be a planar vortex, as long as the anisotropy is above the critical value. For generality, we can consider the size of the hole to be as small as that for a single vacancy ($r_0 \approx a$), or any size larger than this.

III. CONTINUUM CALCULATIONS OF THE MAGNON MODES ON AN AFM VORTEX

The continuum equations for the magnons on a square lattice with lattice spacing a are separated Schrodinger-like equations:[3,35]

$$-\nabla^2 \xi + V(r)\; \xi = \left(\frac{\omega}{c}\right)^2 \xi, \quad (2a)$$

$$-\nabla^2 \eta = \left(\frac{\omega}{c}\right)^2 \eta, \quad (2b)$$

where the long-wavelength spin wave velocity is $c^2 = 8(JSa)^2$ and the effective potential for the out-of-plane wavefunction ξ, which governs the optical spin waves, is

$$V(r) = \frac{\Delta}{a^2} - |\nabla \Phi_v|^2 = \frac{\Delta}{a^2} - \frac{q^2}{r^2}. \quad (3)$$

with

$$\Delta = 4\epsilon + 2d. \quad (4)$$

and $\epsilon = 1 - \lambda$. The parameter Δ is a generic dimensionless anisotropy, which determines the gap of the optical spin wave branch. Apparently, there is no potential effect of the vortex on the acoustic spin waves, which are governed by the field for the in-plane oscillations, η. The presence

of the hole, however, can influence the acoustic spin wave scattering.

Due to the presence of the hole at origin, the potential and wavefunction need only be defined in the outer region $r > r_0$. To completely define the problem, the boundary conditions at $r = r_0$ must be specified. If the hole is simply a region cut out of the continuum system of spins, then the spins on the border of the hole have no particular constraint on their oscillatory motions. This means that they are free to vibrate as the rest of the neighboring spins exerts forces on them. This corresponds to a free type of boundary condition at $r = r_0$, applied to both the in-plane (η) and out-of-plane (ξ) (spin wave) magnon fields. In practice, it means that these fields can be set to a nonzero constant at $r = r_0$. Note that, alternatively, a Dirichlet boundary condition ($\eta = \xi = 0$ at $r = r_0$) would require some extra force that literally freezes the spins in the static vortex spin angles on the hole boundary; such a constraint is absent here. For $r \to \infty$, the magnon fields should decay away to zero.

Using polar coordinates (r, φ) in Eq. (2a), out-of-plane wavefunction solutions varying as $\xi(r, \varphi) = \xi(r) \exp(im\varphi)$ can be expected in the general case, where the radial wavefunctions for $r > r_0$ are seen to satisfy

$$\xi^{''} + \frac{1}{x}\xi^{'} + \xi + \left(\frac{q^2 - m^2}{x^2}\right)\xi = 0. \tag{5}$$

Here $x \equiv kr$, with a real wavevector determined from $k = \sqrt{(\frac{\omega}{c})^2 - \frac{\Delta}{a^2}}$, and primes indicate derivatives with respect to x.

The integer m represents the quantized angular momentum or winding number of the mode. For higher angular momentum modes, with $m^2 \geq q^2$, the equation is the standard equation for Bessel's functions, with the order given by

$$\nu = \sqrt{m^2 - q^2}. \tag{6}$$

For $m^2 < q^2$ we have Bessel functions with imaginary order (see Appendix B) . The unbound states occur above the optical gap frequency,

$$\omega_0 = \sqrt{\Delta}\frac{c}{a}, \tag{7}$$

and have the continuum optical dispersion relation $\omega = \sqrt{\omega_0^2 + k^2c^2}$.

The in-plane spin deviations at angular momentum m follow a free-field equation without any potential term due to the vortex, Eq. (2b), whose radial part for the region $r > r_0$ is

$$\eta^{''} + \frac{1}{x}\eta^{'} + \eta - \frac{m^2}{x^2}\eta = 0. \tag{8}$$

Again, primes indicate derivatives with respect to $x \equiv kr$, but with the acoustic dispersion relation $k = \omega/c$ applied.

General scattering radial solutions for equations (5) and (8) are respectively

$$\xi_m(r) = [B_{1m}J_\nu(kr) + B_{2m}N_\nu(kr)], \tag{9}$$

$$\eta_m(r) = [B_{3m}J_m(kr) + B_{4m}N_m(kr)], \tag{10}$$

where B_{jm} $(j = 1, 2, 3, 4)$ are constants. The values of these constants must be determined by the appropriate boundary conditions.

As mentioned above, there is no particular constraint on the spin wave fields at the hole boundary, $r = r_0$ (free boundary conditions). From the physical point of view, the correct boundary condition is determined by the requirement of *no net flux* of spin wave energy into the hole, which is a region absent of spin degrees of freedom. Alternatively stated, the fields must arrange themselves so that the energy flux in the incoming waves (asymptotics like e^{-ikr}) cancels the energy flux in the outgoing waves (asymptotics like e^{ikr}). The large-r asymptotics of the fields implies a unit magnitude for the complex S-matrix, however, the field/energy constraint that controls the boundary conditions must be applied at $r = r_0$.

A. Vortex charge $q = 1$

Here, $\nu = \sqrt{m^2 - 1}$. The exact scattering phase shifts can be found by applying the appropriate Neumann boundary conditions at the hole boundary, $r = r_0$. Considering first $m \geq 1$ and using $d\xi_m(r)/dr = 0$, $d\eta_m(r)/dr = 0$ for $r = r_0$, the radial wavefunctions become

$$\xi_m(r) = B_{1m}\left[J_\nu(kr) - \tan(\tau_\nu(k))N_\nu(kr)\right], \tag{11}$$

$$\eta_m(r) = B_{3m}[J_m(kr) - \tan(\tau_m(k))N_m(kr)], \tag{12}$$

where $\tan(\tau_\nu(k)) = -B_{2m}/B_{1m}$ and $\tan(\tau_m(k)) = -B_{3m}/B_{4m}$. Explicitly

$$\tau_\nu(k) = \arctan\left[\frac{\nu J_\nu(kr_0) - kr_0 J_{\nu+1}(kr_0)}{\nu N_\nu(kr_0) - kr_0 N_{\nu+1}(kr_0)}\right] \tag{13}$$

and

$$\tau_m(k) = \arctan\left[\frac{mJ_m(kr_0) - kr_0 J_{m+1}(kr_0)}{mN_m(kr_0) - kr_0 N_{m+1}(kr_0)}\right], \tag{14}$$

with $\tau_m(k) = \tau_{-m}(k)$. By comparing the asymptotic behavior of these scattered out-of-plane and in-plane magnon wavefunctions with the behavior of a plane wave solution in the absence of a vortex and hole [$J_m(kr)$] we get the phase-shifts. For instance, consider the out-of-plane magnons solutions with $m \geq 1$ at $r \to \infty$ given by

$$\xi_m \propto \sqrt{\frac{2}{\pi kr}}\cos[kr - (\nu + 1/2)\pi/2 + \tau_\nu(k)]. \tag{15}$$

It gives the following phase-shift

$$\delta^{(1)}_{\xi(m)}(k) = \tau_\nu(k) + (\mid m \mid -\nu)\pi/2, \quad \mid m \mid \geq 1. \tag{16}$$

In general these phase-shifts are well behaved in the interval in which k varies from 0 to $1/a$ (for $k > 1/a$ the continuum approximation is not reliable).

The out-of-plane magnon phase-shift for the angular momentum channel $m = 0$ is not usual since $\nu = \pm i$ is an Imaginary number. Therefore, it will be treated only numerically in Sec. IV. However, our analytical calculations show clearly that the contributions of the hole and the vortex to the phase-shifts can be identified. We notice that the phase-shifts of the out-of-plane magnons (optical modes) contain contributions from both the vortex and the hole. For instance, in Eq. 16 the first term of the second member contains coupled contributions of the hole and vortex while the second term contains only vortex contributions. On the other hand, the phase-shifts of the in-plane magnons (acoustic modes) given by $\delta_{\eta(m)}(k) = \tau_m(k)$ have only contributions of the hole. A comparison between the analytical and numerical results will be presented in Sec. IV.

B. Vortex charge $q = 2$

Using the same methods of the anterior subsection and defining $\mu = \sqrt{m^2 - 4}$, we get for the optical modes

$$\delta^{(2)}_{\xi(m)}(k) = \tau_\mu(k) + (\mid m \mid -\mu)\pi/2, \quad \mid m \mid \geq 2, \quad (17)$$

where τ_μ is given by an expression like Eq. 13 but with ν substituted by μ. The same can be done for acoustic modes; $\delta_m(k) = \tau_m(k)$, $(m > 2)$ is given by Eq. 14. For $m = 0$ and $m = 1$, Bessel functions with imaginary order will not be treated here.

IV. NUMERICAL CALCULATION OF THE SPIN WAVE STATES AND PHASE SHIFTS; VORTEX ON A VACANCY

A limited set of the lowest spin wave modes on a pinned in-plane vortex can be found using a circular system defined by a set of classical spins on a square lattice. The same geometry was used in Ref. 23 to determine the anisotropy-dependent stability properties of singly-charged vortices on a vacancy, where it was also shown that a vortex will be attracted to a vacancy. First, the system is centered on a lattice site, whose spin is removed. The single vacancy at the system center then can be considered as a tiny hole, whose radius is on the order of the lattice constant a. We did not consider holes larger than this. Sites within a radius R from the vacancy are included into the system. After choosing a particular easy-plane anisotropy strength (determined by parameters λ and d, see Hamiltonian 1), a single-vortex spin configuration, centered on the vacancy, is relaxed to a local energy minimum. In the work presented here, we always choose adequately strong anisotropy, greater than the "critical anisotropy", see Ref. 23, only due to exchange (parameter values $\lambda < 1$, $d = 0$), so that the relaxed state is a planar AFM vortex.

The general equations for spin fluctuations around a given vortex or other local energy minimum spin configuration on a lattice have been developed in Refs. 4,6. A self-consistent Gauss-Seidel (GS) relaxation procedure[36] was used to determine the small amplitude normal modes of the spins around a relaxed pinned vortex spin configuration. We usually applied the slightly faster synchronous updating of the wavefunctions. In cases where this led to an obviously unstable solution (typically, at large system radius and/or anisotropy strength close to the critical value), the calculation was performed instead by using the sequential or scanning updating of the wavefunction. Dirichlet boundary conditions are assumed at the outer limit of the system, $r = R$. The procedure gives some frequencies and wavefunctions of the discrete problem, starting from the state of lowest frequency and working upwards. Using typical double precision, we are able to calculate as many as 80 modes for systems up to radius $R = 40a$. The process works in the direction of increasing frequency, without discrimination between acoustic and optical modes. In general, any particular mode will have both nonzero in-plane (η) and out-of-plane (ξ) fluctuations. A mode is identified as being from the optical branch if its frequency is above the gap ($\omega > \omega_0$) and if the magnitudes of its ξ-fluctuations are considerably stronger than those of the η-fluctuations. Further distinguishing features of the two branches are discussed below. Some modes above the gap were found difficult to identify as purely acoustic or purely optical; these were not included in the present analysis.

To compare the numerical results of GS relaxation with the continuum theory, next we describe the spin fluctuations for the acoustic and optical modes in a pure system in a uniform antiferromagnetic state (no vortex or vacancy). Understanding of the phases of the fluctuations on the two sublattices is necessary for determining the continuum fields η and ξ from the original lattice spin fields, $\vec{S}_i$, and for identification of a mode as acoustic or optical. Furthermore, the free spin wave dispersion relations $\omega(\mathbf{k})$ are needed to convert the frequencies obtained from the numerical mode relaxation into the equivalent wavevectors $\mathbf{k}$.

A. Free spin waves on a square lattice

To accomplish this task, we assume that the two sublattice spin fields (alternating sites on the square lattice, measured in the laboratory xyz coordinate system) vary spatially as $e^{i\mathbf{k}\cdot\mathbf{r}}$, with amplitudes $\vec{S}_A = S(1, A^y, A^z)$ on the A-sublattice and $\vec{S}_B = S(-1, B^y, B^z)$ on the B-sublattice. Then substitution of these into the discrete lattice equations of motion from Hamiltonian (1) gives the two distinct solutions for the two spin wave branches, with lattice dispersion relations for exchange anisotropy,

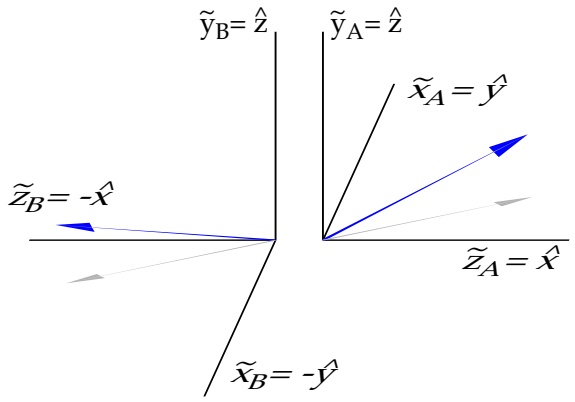

FIG. 1: (color online) Sketch of the local sublattice coordinates, denoted with tildes $(\tilde{x}, \tilde{y}, \tilde{z})$ on sublattices A and B, in a medium of uniform antiferromagnetism. The bold arrows represent the fluctuating spins, relative to the uniform AFM state, in the phase relationships expected for an acoustic spin wave mode. The faint arrows reference the laboratory xy plane.

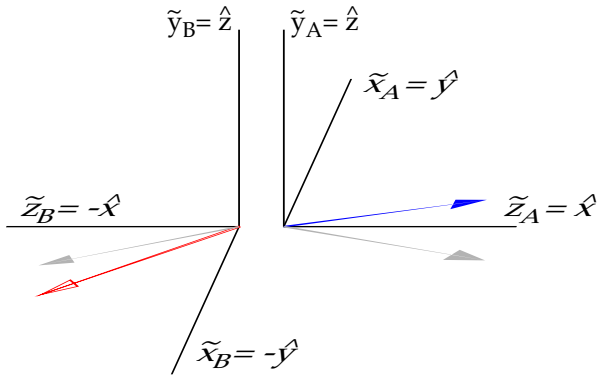

FIG. 2: (color online) Sketch of the local sublattice coordinates, denoted with tildes $(\tilde{x}, \tilde{y}, \tilde{z})$ on sublattices A and B, in a medium of uniform antiferromagnetism. The bold arrows represent the fluctuating spins, relative to the uniform AFM state, in the phase relationships expected for an optical spin wave mode. The faint arrows reference the laboratory xy plane. The open arrow (red online) tilts below the xy plane.

$$\omega_{\mathbf{k}} = 4JS\sqrt{(1 \mp \gamma_{\mathbf{k}})(1 \pm \lambda\gamma_{\mathbf{k}})}, \tag{18}$$

where upper (lower) signs here and in subsequent equations are for the acoustic (optical) branches, and

$$\gamma_{\mathbf{k}} = \frac{1}{2}\left(\cos k_x a + \cos k_y a\right). \tag{19}$$

Assuming propagation along $\hat{x}$, as $\vec{k} = (k, 0)$, then one has $k = \cos^{-1}(2\gamma_{\mathbf{k}} - 1)$, where $\gamma_{\mathbf{k}}$ is obtained from the frequency, using (18), as

$$\gamma_{\mathbf{k}} = (2\lambda)^{-1}\{\mp(1-\lambda) + \sqrt{(1-\lambda)^2 + 4\lambda[1 - (\omega/4JS)^2]}\}. \tag{20}$$

In addition to this relation for determining k, the spin wave analysis determines the relative phases of the different spin components. As in previous articles on this topic,[4,6,36] it is convenient to use local spin coordinates $(S_n^{\tilde{x}}, S_n^{\tilde{y}}, S_n^{\tilde{z}})$ at each lattice site, oriented so that the axis $\tilde{z}_n$ is placed along the relaxed static spin direction, while $\tilde{x}_n$ lies within the laboratory xy-plane, and finally $\tilde{y}_n = \tilde{z}_n \times \tilde{x}_n$, forming a right handed set. In this notation, the fluctuations $S_n^{\tilde{x}}$ take place within the laboratory xy-plane, while the fluctuations $S_n^{\tilde{y}}$ correspond to out-of-plane motions, see Figs. 1 and 2. Each static spin has $S_n^{\tilde{z}} = S$, regardless of its sublattice.

1. *Square lattice acoustic modes*

For the acoustic modes, with $\omega \to 0$ as $k \to 0$, the laboratory spin components on the two sublattices are found to have the phase relationships,

$$\vec{S}_A = S(1, A^y, A^z), \quad \vec{S}_B = S(-1, -A^y, A^z). \tag{21}$$

The combination of in-plane components out-of-phase, with out-of-plane components in-phase, becomes simpler if one looks at the local spin components, as suggested in Fig. 1. The local spin component fluctuations are seen to have the relations,

$$S_A^{\tilde{x}} = S_B^{\tilde{x}}, \quad S_A^{\tilde{y}} = S_B^{\tilde{y}}, \tag{22}$$

that is, the local spin components on the two sublattices move together, in-phase. The amplitude relationship between in-plane and out-of-plane local components on one sublattice, furthermore, shows a predominant in-plane vibration, and a 90° phase relation,

$$A^z = \frac{-i\omega}{4JS(1+\lambda\gamma_{\mathbf{k}})}A^y \approx \frac{-ika}{2\sqrt{1+\lambda}}A^y. \tag{23}$$

As $k \to 0$, the out-of-plane fluctuations vanish. Modes found in the numerical relaxation for the vortex-on-vacancy problem, with these typical characteristics, can be expected to belong to the acoustic branch.

2. *Square lattice optical modes*

In the optical modes, with finite frequency as $k \to 0$, the laboratory spin components again have a mixed phase relationship between the sublattices,

$$\vec{S}_A = S(1, A^y, A^z), \quad \vec{S}_B = S(-1, A^y, -A^z). \tag{24}$$

In this case, when written in terms of the local spin components, (Fig. 2) there is a purely out-of-phase relationship between the sublattices:

$$S_A^{\tilde{x}} = -S_B^{\tilde{x}}, \quad S_A^{\tilde{y}} = -S_B^{\tilde{y}}. \tag{25}$$

The amplitude relationship between in-plane and out-of-plane components on an individual sublattice shows a 90° relationship, together with a predominant out-of-plane motion,

$$A^z = \frac{-i\omega}{4JS(1-\lambda\gamma_{\mathbf{k}})} A^y \approx -i\sqrt{\frac{2}{1-\lambda}} A^y. \tag{26}$$

The latter form results from the limiting dispersion relation (gap frequency), $\omega(0) = \omega_0 = 2JS[8(1-\lambda)]^{1/2}$. Especially in the region of weak easy-plane anisotropy ($\lambda \approx 1$), the out-of-plane vibrations are enhanced. Modes from the numerical diagonalization for the vortex-on-vacancy problem, with these kinds of characteristics, will be considered as belonging to the optical branch.

3. *Mapping onto the continuum fields*

The numerical mode relaxation procedure calculates the local in-plane ($S_n^{\tilde{x}}$) and out-of-plane ($S_n^{\tilde{y}}$) spin fields. In going over to the continuum limit for equations (2), one finds the relations between the discrete and continuum fields as[35]

$$S_A^{\tilde{x}} \approx \eta + \frac{1}{8JS}\frac{\partial \xi}{\partial t}, \quad S_A^{\tilde{y}} \approx -\xi + \frac{1}{8JS}\frac{\partial \eta}{\partial t}, \tag{27a}$$

$$S_B^{\tilde{x}} \approx \eta - \frac{1}{8JS}\frac{\partial \xi}{\partial t}, \quad S_B^{\tilde{y}} \approx \xi + \frac{1}{8JS}\frac{\partial \eta}{\partial t}, \tag{27b}$$

Generally, the second terms in these expressions can be ignored, to leading order, because we are analyzing low-frequency modes with $\omega \ll 8JS$. Then, the η-field is derived from the smooth variations in the in-plane ($S^{\tilde{x}}$) local components, while the ξ-field is derived from the staggered variations in the out-of-plane ($S^{\tilde{y}}$) local components. The staggered variations can be defined by taking -1 times the A-sublattice values, and $+1$ times the B-sublattice values. Clearly, these mappings show the generally acoustic nature of the η-field, and the generally optical nature of the ξ-field. They also suggest, however, the possibility of a mixing between acoustic and optical motions, which sometimes makes it impossible to identify a mode as purely acoustic or purely optical.

B. Numerical Mode Spectra, $q = 1$ Vortex-on-vacancy

We consider a single $q = 1$ planar vortex pinned on a vacancy at the system center. The numerical relaxation procedure[36] was applied for anisotropy constant

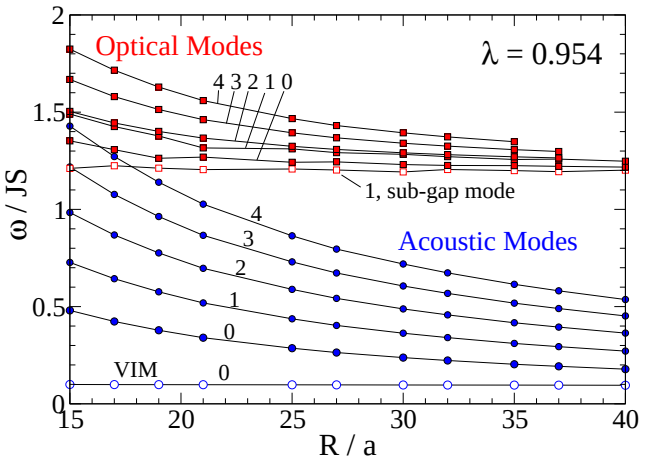

FIG. 3: (Color online) Partial mode spectrum for $\lambda = 0.954$. Integer numbers by data curves indicate the azimuthal quantum numbers m. The gap frequency is $\omega_0/JS \approx 1.213$. Only the lowest scattering modes at each m, for each branch, are shown. The VIM and *sub-gap mode* occur at relatively constant frequency, while usual scattering modes have a dependence on $1/R$.

$\lambda = 0.90, 0.95, 0.954$, values approaching the vortex-on-vacancy critical anisotropy,[23] $\lambda_{cv} \approx 0.9545$, below which the vortex remains planar. In order to get a range of possible wavevectors k, the calculations were performed for a range of system sizes between $R = 15a$ and $R = 40a$. Up to the lowest 80 modes were found for each system. To go to larger systems is possible, but the computational time becomes excessive. To go to many more modes is not possible, because the accumulation of numerical errors eventually leads to instability in the calculation. Generally speaking, very few optical modes could be found for the larger systems, because the acoustic mode frequencies generally fall lower and lower as the system size is increased, pushing the optical modes up out of the lowest 80.

1. *Modes at* $\lambda = 0.954$

At anisotropy strength very close to the critical value ($\lambda_{\rm cv} \approx 0.9545$), the spectrum takes it simplest form, because the VIM occurs at a frequency lower than all of the other modes, for the system sizes studied. The frequencies of some of the lowest acoustic and optical modes are shown in Fig. 3, as functions of the system radius R. The usual scattering states have typical $e^{\pm im\varphi}$ spatial dependence, for example, for $R = 15a$, the lowest $m = 1$ acoustic mode and lowest $m = 2$ optical mode are shown in Figs. 4 and 5. The unfilled (filled) arrows in these figures indicate the complex $S^{\tilde{x}}$ ($S^{\tilde{y}}$) fluctuating spin components. ($S^{\tilde{x}}$ are in-plane fluctuations, $S^{\tilde{y}}$ are out-of-plane fluctuations.) The differences between acoustic and optical mode wavefunctions are apparent.

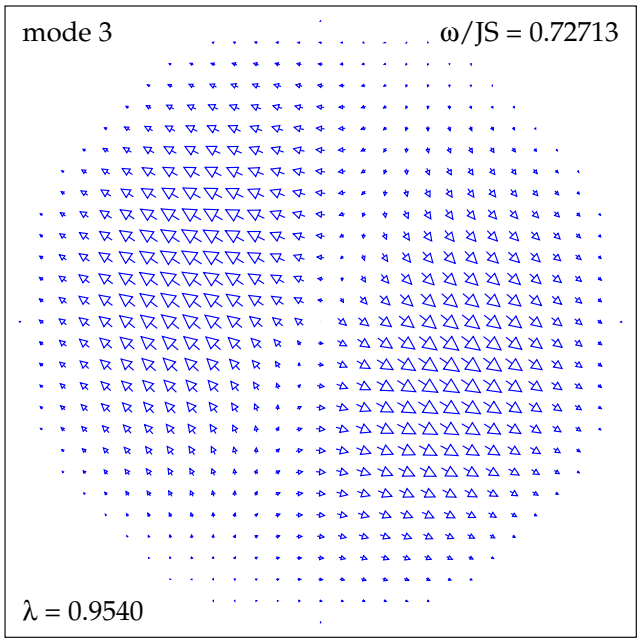

FIG. 4: (Color online) Lowest $m = 1$ acoustic mode wavefunction ($S^{\tilde{x}}$) for $\lambda = 0.954$, in a system of radius $R = 15a$. In-plane oscillations of the spins are represented by arrows with unfilled triangular heads (blue online), whose magnitudes and directions give the complex amplitudes, $S^{\tilde{x}}$. The negligible out-of-plane oscillation component for this mode is not shown.

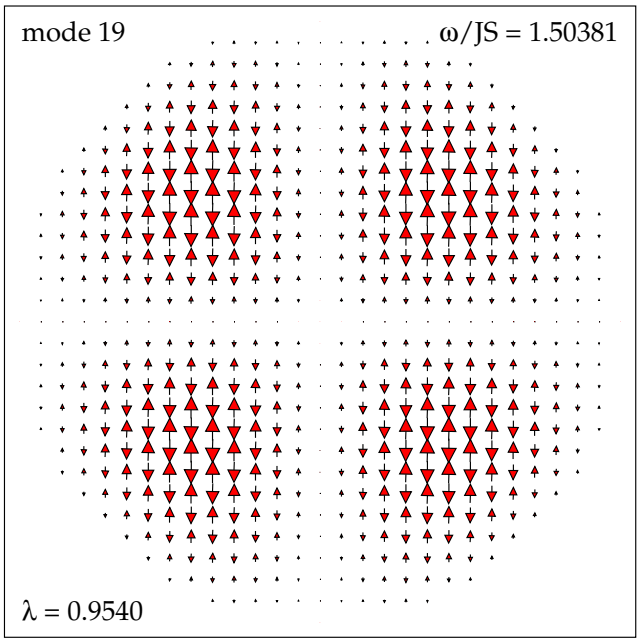

FIG. 5: (Color online) Lowest $m = 2$ optical mode wavefunction ($S^{\tilde{y}}$) for $\lambda = 0.954$, in a system of radius $R = 15a$. Out-of-plane oscillations of the spins are represented by arrows with filled triangular heads (red online), whose magnitudes and directions give the complex amplitudes, $S^{\tilde{y}}$. For this and most of the optical branch states, the in-plane oscillation component is negligible and is not shown.

Scattering modes at other m have similar appearances, but with a different number of lobes depending on m. From observation of the wavefunctions, the values of m can be assigned.[37] Then the scattering phase shifts can be calculated as described below.

The instability mode (VIM) takes a dramatic form, Fig. 6, characterized by a wavefunction dominated by out-of-plane fluctuations concentrated near the vortex core, with circular symmetry ($m = 0$). The exponential decay of the VIM wavefunction with radius leads to a low frequency nearly independent of the system size, determined primarily by the anisotropy strength and the size of the hole on which the vortex is pinned. Although it is well below the optical gap, its vibrations are like that of an optical mode. It is a localized bound state, hence, there is no scattering analysis for its out-of-plane field. The properties are further analyzed in Sec. V.

Just below the optical gap frequency ω_0, another unusual state occurs with nearly size-independent frequency, and quantum number $m = 1$. It has been marked in Fig. 3 as the *sub-gap mode*. A wavefunction structure is shown in Fig. 7; although its frequency is below the gap, its structure is that of an optical mode: strong out-of-plane fluctuations that are out of phase on the two sublattices. This state is interesting because it is always the lowest frequency mode that appears to belong to the optical branch. Yet, we are not able to calculate a scattering phase shift for this state, because it is not possible to assign a value for the wavevector k by using Eq. (20), which requires $\omega > \omega_0$. It seems likely that the mode is indeed the lower limit of the optical branch, whose gap has been reduced by the vortex-hole interactions. It is not otherwise analyzed in this work.

2. *Modes at* $\lambda = 0.95$ *and* $\lambda = 0.90$

At anisotropy strength $\lambda = 0.95$, farther from the critical value ($\lambda_{\rm cv} \approx 0.9545$), the spectrum is somewhat different, because the VIM frequency now moves up into the acoustic branch spectrum for the system sizes studied. The frequencies of some of the lowest acoustic and optical modes are shown in Fig. 8, as functions of the system radius R. The gap has increased slightly compared to that for $\lambda = 0.954$, but this has no significant effect on the modes. Primarily, the higher frequency VIM mixes with acoustic states, and in this sense, it is not really possible to say that there is an individual VIM state. Various modes low in the spectrum have the appearance of strong out-of-plane oscillations near the vortex core, together with circular symmetry. At system radius $R = 20a$, for example, the two lowest modes' wavefunctions, shown in Fig. 9 and Fig. 10, both exhibit strong centralized out-of-plane oscillations, but with different phases compared to the in-plane fluctuations. The

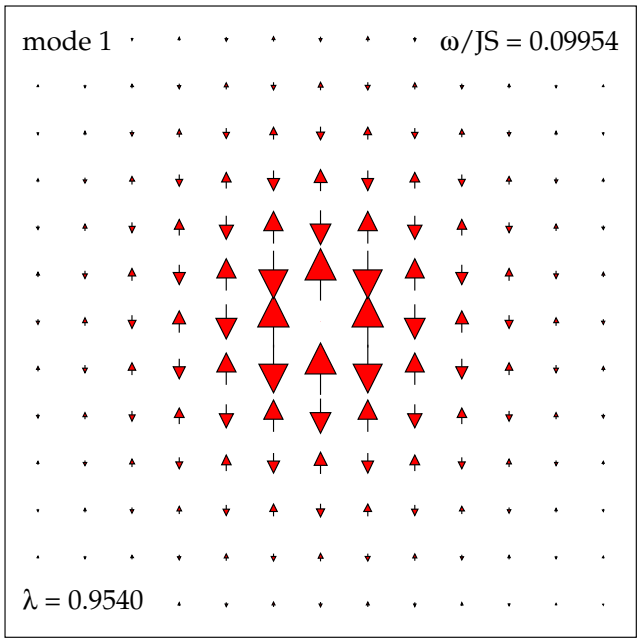

FIG. 6: (Color online) Central region of the vortex instability mode (VIM) wavefunction for $\lambda = 0.954$, in a system of radius $R = 15a$, using arrows as in Fig. 5. Only the out-of-plane field, $S^{\tilde{y}}$ is shown; the in-plane component is negligible. Although well below the optical gap, $\omega_0/JS \approx 1.213$, the structure is that of an optical mode. The wavefunction amplitudes are concentrated near the vortex core, with a length-scale that depends on the hole size and anisotropy strength.

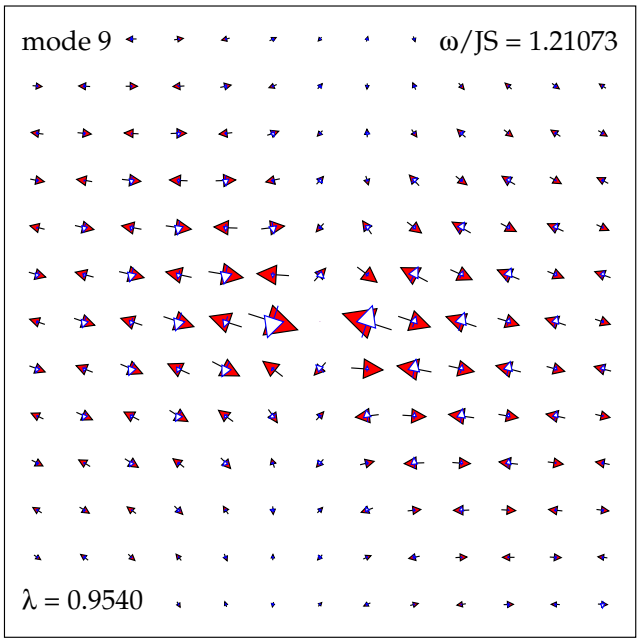

FIG. 7: (Color online) Central region of the sub-gap $m = 1$ optical mode wavefunction for $\lambda = 0.954$, in a system of radius $R = 15a$. Unfilled (filled) arrows describe in-plane or $S^{\tilde{x}}$ (out-of-plane or $S^{\tilde{y}}$) spin fluctuations. This mode typically maintains a nearly constant frequency just below ω_0 as R is changed.

in-plane fluctuation components also have different radial dependence. With increasing system size, different modes take on the appearance of the strong out-of-plane centralized oscillations. Generally, other higher-m modes have appearances similar to those in the wavefunction plots for $\lambda = 0.954$.

At even stronger easy-plane anisotropy, $\lambda = 0.90$, both the gap and the VIM frequency increase substantially, see Fig. 11 for a partial spectrum versus system radius. Several $m = 0$ modes in the acoustic frequency range have strong out-of-plane oscillations centralized on the vortex core, being indicated as VIM-like on Figure 11. Because of the larger gap, the calculation of the optical mode spectrum becomes rather difficult; fewer modes of the optical branch can be determined by the GS relaxation procedure. A sub-gap mode, however, is still present. Whether this mode is present when there is no vacancy cannot be determined; an anisotropy parameter as low as $\lambda \approx 0.70$ would have to be used (the critical value without a vacancy), but this would lead to such a large gap frequency, that no optical modes can be easily calculated.

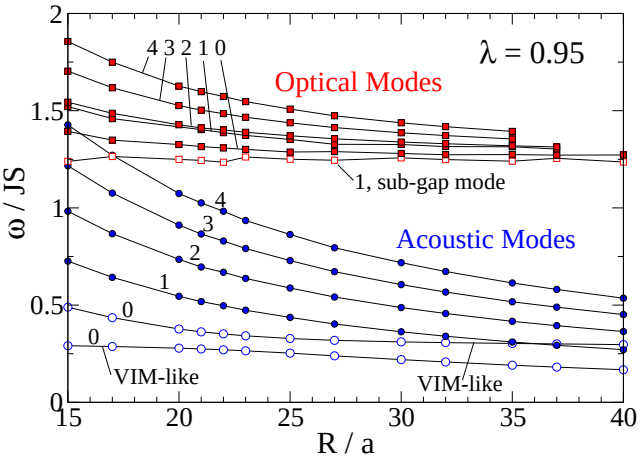

FIG. 8: (Color online) Partial mode spectrum for $\lambda = 0.95$, following the notations of Fig. 3. The gap frequency is $\omega_0/JS \approx 1.265$. Now the two lowest $m = 0$ modes have a centralized strong out-of-plane oscillation, or VIM-like properties.

C. Scattering States and Phases Shifts, $q = 1$ Vortex-on-vacancy

Depending on the assigned value of azimuthal quantum number m, as obtained from the wavefunctions, together with identification as an acoustic or optical mode, some-

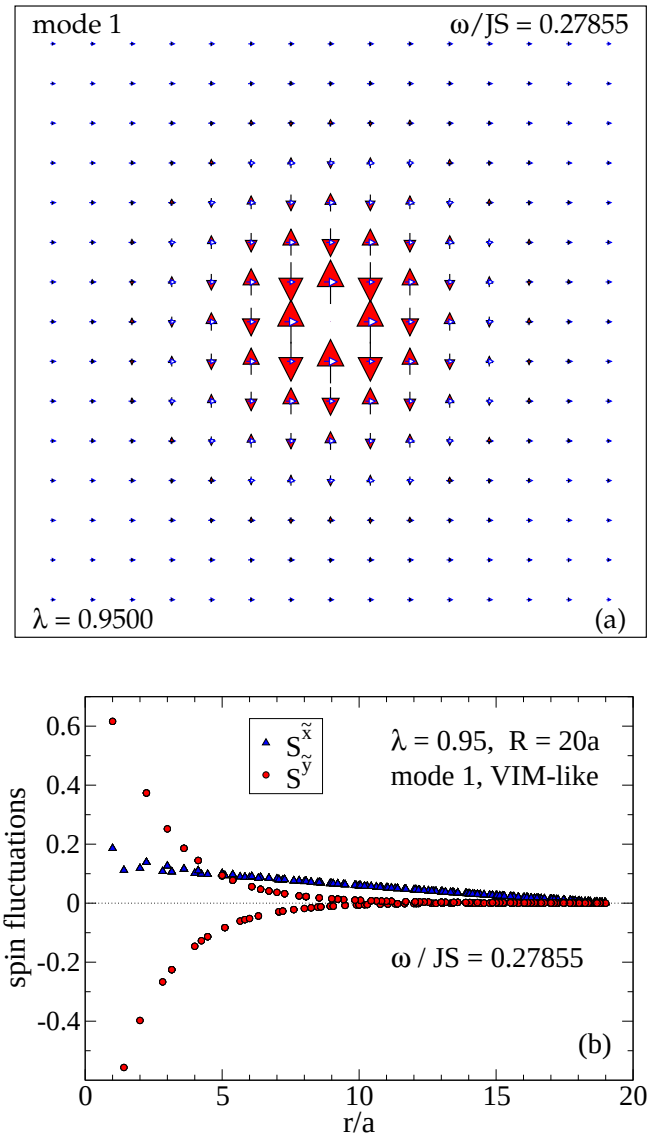

FIG. 9: (Color online) Central region of the lowest mode wavefunction for $\lambda = 0.95$, $R = 20a$, (a) following the notations of Fig. 7 and (b) showing the radial structure. This mode exhibits a centralized strong out-of-plane oscillation, or VIM-like structure, in combination with moderately strong in-plane oscillations.

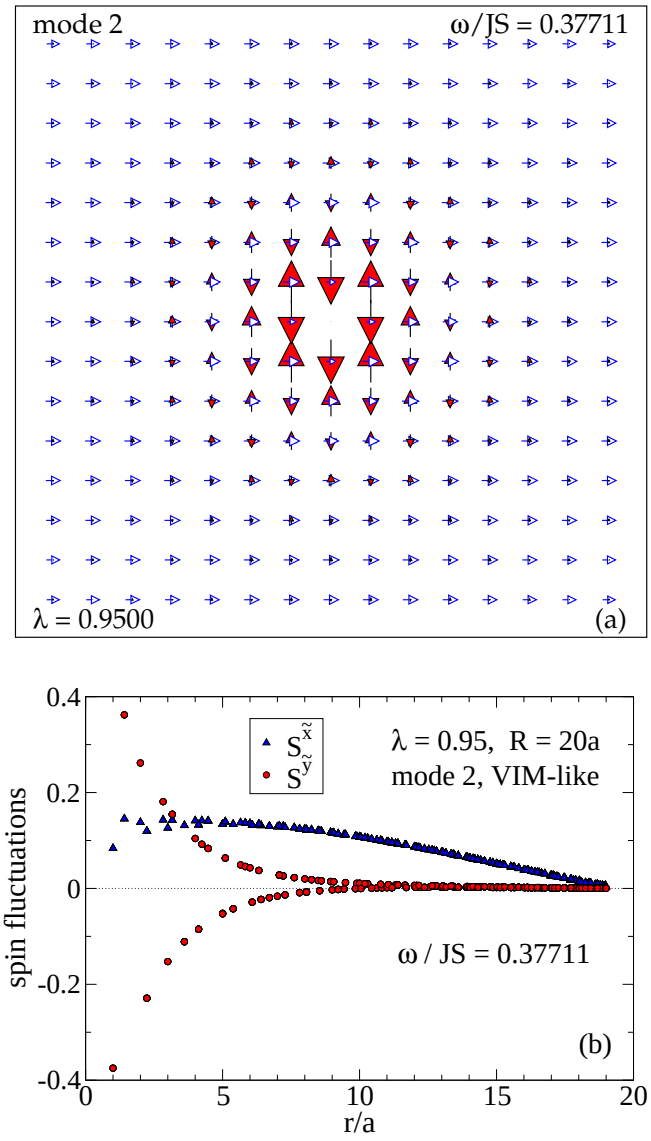

FIG. 10: (Color online) Central region of the second lowest mode wavefunction for $\lambda = 0.95$, $R = 20a$, (a) following the notations of Fig. 7 and (b) showing the radial structure. This mode also exhibits a centralized strong out-of-plane oscillation, or VIM-like structure, in combination with relatively strong in-plane oscillations. Note that the phase relationships between the in-plane and out-of-plane components are different here than for mode 1, Fig. 9.

what different analysis was applied to the wavefunctions, to extract the scattering phase shifts.

1. *Wavefunction fittings for $m^2 \geq q^2$*

With the exception of the optical modes where $m^2 < q^2$, the determination of the scattering phase shifts follows standard procedures, summarized here. For the acoustic modes, the in-plane field obtained from the numerics is fitted to the form,

$$\begin{aligned} \eta(r,\varphi) &= [a_1 J_m(kr) + b_1 N_m(kr)]\, e^{im\varphi} \\ &+ [a_2 J_m(kr) + b_2 N_m(kr)]\, e^{-im\varphi}. \end{aligned} \quad (28)$$

The combination of $\pm m$ modes is necessary due to their approximate degeneracy on a square lattice.[7] The constants a_1, b_1, a_2, b_2 were determined by a least squares fitting, Appendix A, of the entire wavefunction data to this functional form. This then defines scattering ampli-

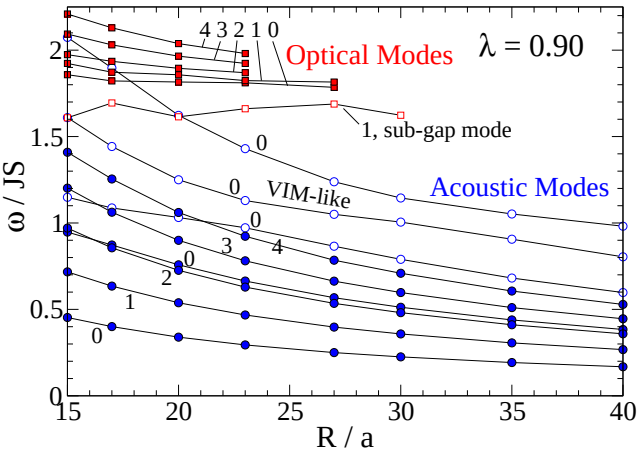

FIG. 11: (Color online) Partial mode spectrum for $\lambda = 0.9$, following the notations of Fig. 3. The gap frequency is $\omega_0/JS \approx 1.789$. Now various $m = 0$ modes in the acoustic spectral range have a centralized strong out-of-plane oscillation, or VIM-like properties.

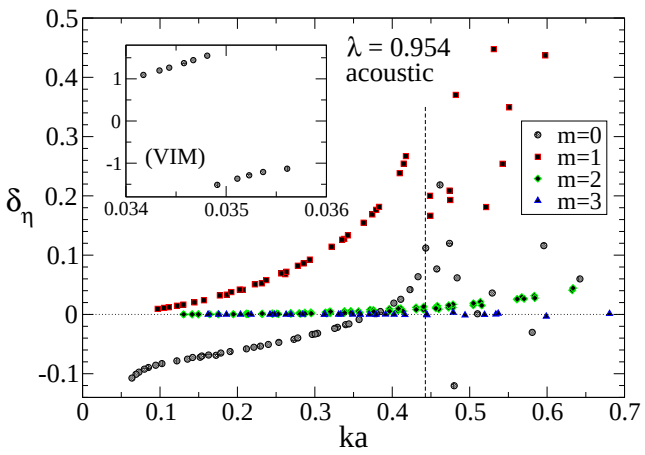

FIG. 12: (Color online) Acoustic mode scattering phase shifts versus wavevector for $\lambda = 0.954$, at the indicated angular momentum values m. The inset shows the analysis of the in-plane oscillations of the vortex instability mode, which occur at significantly lower frequency. The dashed vertical line indicates the wavevectors beyond which the acoustic spectrum overlaps with the optical spectrum. Modes to the right of this line may have optical as well as acoustic properties.

tudes,

$$\rho_m(k) = b_1/a_1, \quad \rho_{-m} = b_2/a_2, \tag{29}$$

which should be nearly identical and real. The large-r asymptotic form of η for a single angular momentum results from the asymptotics of the Bessel functions, and gives an amplitude that can be written as a sum of an incident wave and a modified scattered wave,

$$\eta_m(r \to \infty) \sim \sqrt{\frac{1}{2\pi kr}} \left[e^{-i(kr-\phi_m)} + S_m(k) e^{i(kr-\phi_m)} \right]. \tag{30}$$

The Bessel phase is $\phi_m \equiv \frac{\pi}{4}(2m+1)$. The scattering phase shift $\delta_m(k)$ of the outgoing wave compared to the incoming wave is related to the S-matrix and scattering amplitudes, according to

$$S_m(k) = \frac{1 - i\rho_m(k)}{1 + i\rho_m(k)} = e^{2i\delta_m(k)}. \tag{31}$$

Then, the scattering phase shift is found to be

$$\delta_m(k) = -\tan^{-1} \rho_m(k). \tag{32}$$

The same analysis applies to the calculation of the scattering phase shifts for the optical modes, as does Eq. (32), but using the data for the ξ-field, and fitting to Bessel functions of order $\nu = \sqrt{m^2 - q^2}$ in Eq. (28), which need not be integer.

Applying the above described analysis, the scattering phase shifts δ_η for $\lambda = 0.954$, for modes in the acoustic spectrum, are shown in Fig. 12. The points on these and similar graphs below were obtained from calculations on lattices of radii ranging from $R = 15a$ to $R = 50a$, in order to produce sets of data over a wide enough range of k.

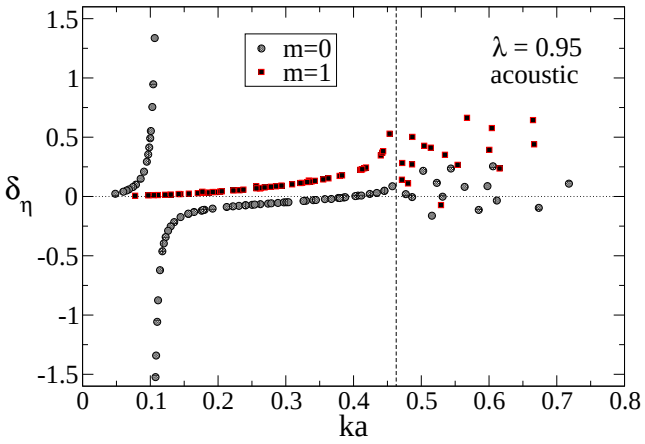

FIG. 13: (Color online) Acoustic mode scattering phase shifts versus wavevector for $\lambda = 0.95$, in the notation of Fig. 12. The modes where the $m = 0$ scattering passes $\pi/2$ have VIM-like structure.

A dashed vertical line has been placed at the value of ka corresponding to the wavevector above which the acoustic branch frequencies overlap with the optical branch frequencies. Generally, the data beyond this point come from modes that appear to be acoustic, but still have significant influence of the optical states. As such, these data do not follow a simple trend.

The strongest acoustic scattering effects take place at $m = 0$ and $m = 1$; there is very weak scattering at higher angular momenta. The inset of Fig. 12 shows the analysis even including the VIM; its in-plane wavefunction was used in the analysis, even though it is dominated by its

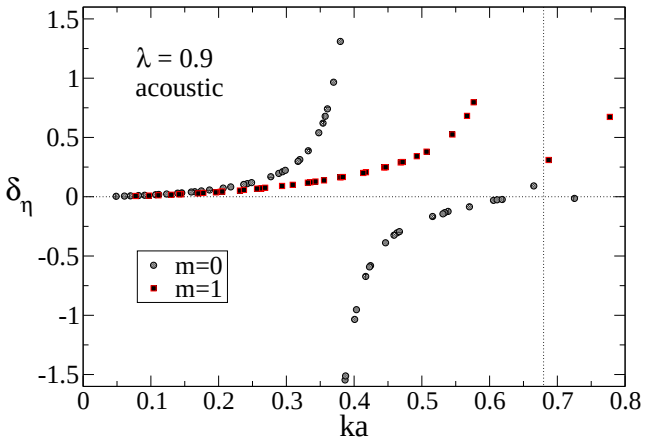

FIG. 14: (Color online) Acoustic mode scattering phase shifts versus wavevector for $\lambda = 0.90$, in the notation of Fig. 12.

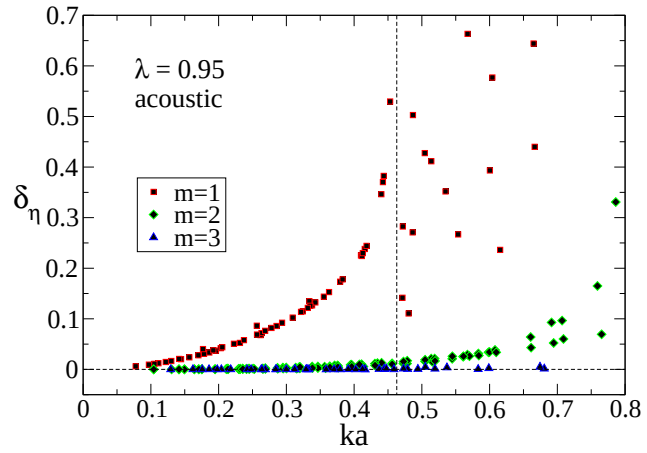

FIG. 15: (Color online) Acoustic mode scattering phase shifts versus wavevector for $\lambda = 0.95$, in the notation of Fig. 12, comparing modes with $m > 0$.

out-of-plane component. It is intriguing to note that the $m = 0$ phase shift passes through π (or equivalently, $-\pi$) at a finite but small wavevector, see the VIM inset. That this is indeed a general phenomenon at $m = 0$, can be seen by comparing with the corresponding results at $\lambda = 0.95$ and $\lambda = 0.90$, shown in Fig. 13 and Fig. 14. Again, including the modes with VIM-like structure, the $m = 0$ scattering phase shift passes through π at a finite value of ka, and eventually through zero at a higher value of ka. The scattering at $\lambda = 0.95$ for $m > 0$ is shown in Fig. 15. There is again a moderate scattering effect for $m = 1$ only, and very little at higher m. The same holds for $\lambda = 0.90$.

A comparison between these results for the acoustic modes with the simple analytical approximation of Sec. III [see Eq. 14] shows that the continuum theory works very well for $m \neq 0$. In fact, there is a good qualitative and even quantitative agreement between the numerical

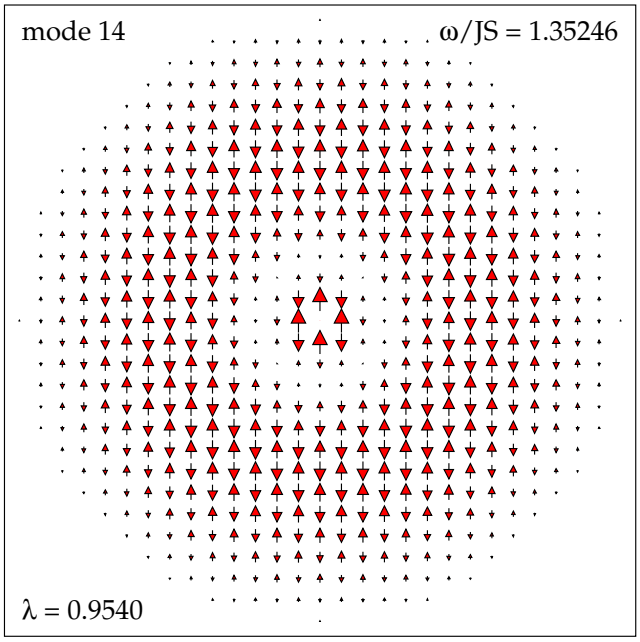

FIG. 16: (Color online) Lowest $m = 0$ above-gap optical mode wavefunction ($S^{\tilde{y}}$) for $\lambda = 0.954$, in a system of radius $R = 15a$. The meaning of the arrows is given in Fig. 5; the negligible $S^{\tilde{x}}$ field is not shown. There is always at least one nodal ring surrounding the central core region for these states.

and analytical results for angular momentum channels $| m | > 0$. However, the analytical result is completely different from our numerical analysis in the case $m = 0$. This disagreement may be justified by the fact that this particular wave (s wave) can approach the zone of strong influence of the hole, which involve small scale and hence the continuum theory should be viewed with caution. We will return to this discussion after treating the optical modes. For now we just remember that $m = 0$ modes were not considered in the continuum theory for the out-of-plane magnons (optical modes).

2. *Wavefunction fittings for $m = 0$ at $q = 1$*

For vortex charge $q = 1$, the $m = 0$ optical modes are unusual, in that their analysis involves the use of Bessel functions of imaginary order, $\nu = i$, see Sec. III. A typical wavefunction obtained numerically is shown in Fig. 16. The functions $J_i(x)$ and $N_i(x)$, defined by appropriate power series and other relations, Appendix B, are complex, unlike the (real) Bessel functions at real order. In order to develop a definition of the scattering phase shift, one needs to interpret the ξ-wavefunction as composed from a linear combination of incoming incident wave together with a scattered outgoing wave, using the asymptotics of these Bessel functions.

The ξ-field from the numerical relaxation is fitted by a least squares procedure, Appendix A, to the functional

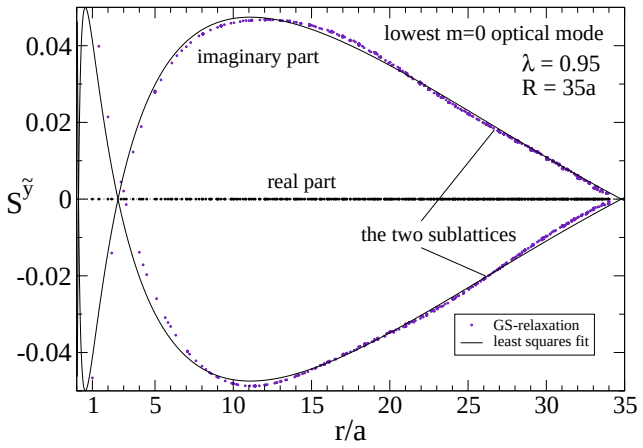

FIG. 17: Lowest $m = 0$ above-gap optical mode radial wavefunction for $\lambda = 0.95$, in a system of radius $R = 35a$, with frequency $\omega = 1.2742JS$ and wavevector $ka = 0.056475$. Data symbols show calculations on a square lattice using the numerical GS-relaxation method; solid curves are least square fits to Eq. (33). The complex fitting parameters are $a_1 = (0.09126723, 0.1231743)$ and $b_1 = (0.1129695, -0.09951148)$, leading to $\rho_0 = (-0.082838, -0.978532)$ and scattering phase shift $\delta_0 = 0.679533$, using (40).

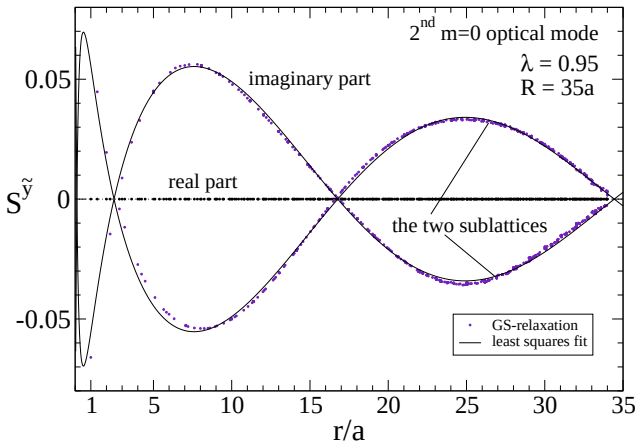

FIG. 18: Second lowest $m = 0$ above-gap optical mode radial wavefunction for $\lambda = 0.95$, in a system of radius $R = 35a$, with frequency $\omega = 1.3482JS$ and wavevector $ka = 0.172089$. The complex fitting parameters for Eq. (33) are $a_1 = (-0.06647212, 0.2149658)$ and $b_1 = (0.1971564, 0.07247664)$, leading to $\rho_0 = (0.048877, -0.932266)$ and scattering phase shift $\delta_0 = -0.325185$, using (40).

form,

$$\xi(r,\varphi) \;=\; [a_1 J_i(kr) + b_1 N_i(kr)]\,, \tag{33}$$

leading to the complex amplitude coefficient, $\rho_0(k) = b_1/a_1$. For example, the quality of such fittings is shown in Fig. 17 for the lowest $m = 0$ optical mode for a system with $\lambda = 0.95$ and $R = 35a$, which has frequency $\omega = 1.2742JS$, corresponding to a wavevector $ka = 0.056475$. The graph shows the out-of-plane spin fluctuations, $S^{\tilde{y}}$; the staggered values on the sublattices defines ξ. This mode is very similar in structure to that shown in Fig. 16. These wavefunctions are pure imaginary, as indicated by the vertically oriented arrows for $S^{\tilde{y}}$. The fitted function (solid curves in Fig. 17) is for all practical purposes, pure imaginary; there are opposite signs of the imaginnary part of $S^{\tilde{y}}$ on the two sublattices. Note that there are no data within the hole $r < a$, although the fitted curve is shown there. Another example of the accuracy of these fittings is displayed in Fig. 18, for the second lowest $m = 0$ optical mode, of the same system, which has frequency $\omega = 1.3482JS$, corresponding to wavevector $ka = 0.172089$. This is essentially the same scattering state, but observed at a higher energy and wavevector.

Once a fit to any state has been accomplished, we consider how the fitted value of ρ_0 determines a corresponding value of scattering phase shift. Importantly, the state $\xi \sim J_i$, with $\rho_0(k) = 0$, is not a state of zero scattering, as can be seen from the asymptotics of these Bessel functions at large argument $x \equiv kr \gg 1$:

$$J_i(x) \approx \sqrt{\frac{1}{2\pi x}}\left[e^{-\frac{\pi}{2}} e^{-i(x-\frac{\pi}{2})} + e^{\frac{\pi}{2}} e^{i(x-\frac{\pi}{4})}\right], \tag{34a}$$

$$N_i(x) \approx i\sqrt{\frac{1}{2\pi x}}\left[e^{-\frac{\pi}{2}} e^{-i(x-\frac{\pi}{2})} - e^{\frac{\pi}{2}} e^{i(x-\frac{\pi}{4})}\right]. \tag{34b}$$

In each of these functions, the outgoing wave $[e^{i(x-\frac{\pi}{4})}]$ is stronger in amplitude than the incoming wave, hence neither could represent a state of no scattering. Using these expressions, we can construct a state $\xi_{\rm NS}$, that corresponds to no scattering, by a linear combination with synchronized equal-amplitude in and out waves,

$$\xi_{\rm NS} \;\approx\; \sqrt{\frac{1}{2\pi x}}\left[e^{-i(x-\frac{\pi}{4})} + e^{i(x-\frac{\pi}{4})}\right], \tag{35}$$

$$\xi_{\rm NS} \;\to\; \sqrt{\frac{2}{\pi x}}\left[\cosh\left(\frac{\pi}{2}\right) J_i(x) - i\sinh\left(\frac{\pi}{2}\right) N_i(x)\right].$$

The latter form corresponds to the analytic continuation of the asymptotic expression. It shows that a zero scattering state has the pure imaginary coefficient, $\rho_{\rm NS} = -i\tanh\frac{\pi}{2}$. Extending this idea to states where scattering takes place, with scattering S-matrix, $S_0(k) = e^{2i\delta_0(k)}$ different from unity, the ξ-field can be expected to have the asymptotic form,

$$\xi_0 \approx \sqrt{\frac{1}{2\pi x}}\left[e^{-i(x-\frac{\pi}{4})} + S_0(k) e^{i(x-\frac{\pi}{4})}\right], \tag{36}$$

which is analytically continued to all r by the expression

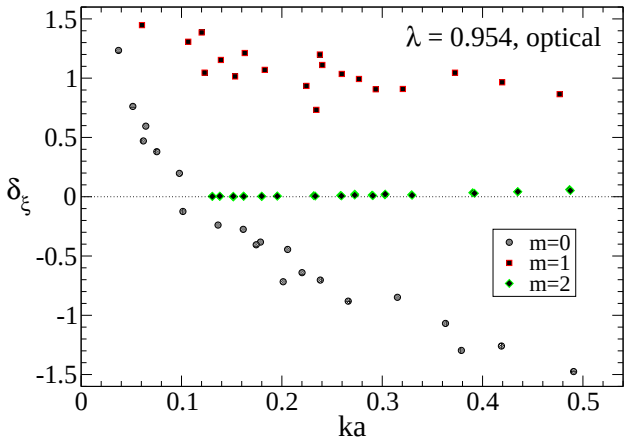

FIG. 19: (Color online) Optical mode scattering phase shifts versus wavevector for $\lambda = 0.954$, at the indicated angular momentum values m.

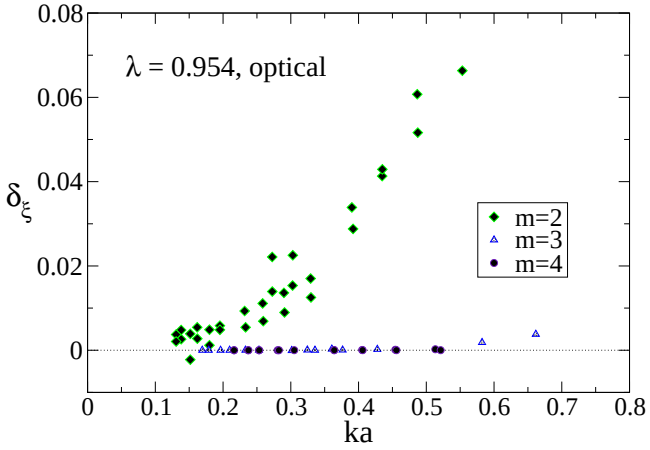

FIG. 20: (Color online) Optical mode scattering phase shifts versus wavevector for $\lambda = 0.954$, at the indicated angular momentum values m.

$$\xi_0(r) = \frac{e^{\frac{\pi}{2}} + S_0(k)e^{-\frac{\pi}{2}}}{2} J_i(kr) - i\frac{e^{\frac{\pi}{2}} - S_0(k)e^{-\frac{\pi}{2}}}{2} N_i(kr) \tag{37}$$

The latter result correctly reduces to (35) in the no scattering limit, $S_0(k) \to 1$.

The result (37) determines $\rho_0(k)$ in terms of $S_0(k)$, from which the scattering phase shift can be found:

$$S_0(k) = e^{\pi}\left[\frac{1 - i\rho_0(k)}{1 + i\rho_0(k)}\right] = e^{2i\delta_0(k)}. \tag{38}$$

The physical requirement of energy conservation in the scattering process implies $|S_0(k)|^2 = 1$. This then places a constraint on the real and imaginary parts of $\rho_0(k)$,

$$\mathrm{Im}[\rho_0(k)] = -\frac{1}{2}\tanh(\pi)\left[1 + |\rho_0(k)|^2\right]. \tag{39}$$

It forces the imaginary part to be more negative than $-\frac{1}{2}\tanh(\pi)$, providing a check on the calculations. Eq. (38) leads to the phase shift,

$$\delta_0(k) = -\frac{1}{2}\tan^{-1}\left\{\frac{2\ \mathrm{Re}[\rho_0(k)]}{1 - |\rho_0(0)|^2}\right\}. \tag{40}$$

One can note, in fact, that this last equation also applies to all the phase shifts at non-zero m, as it reduces to (32) when ρ is pure real.

The resulting scattering phase shifts δ_ξ for $\lambda = 0.954$, for modes in the optical spectrum, are shown in Fig. 19 and Fig. 20. At $m = 0$, the scattering phase shift ranges from $+\pi/2$ at small k, passing through zero at $ka \approx 0.12$, until finally approaching $-\pi/2$ for larger k. The phase shift at $m = 1$ apparently falls slowly from $\pi/2$ at small k and possibly drifts towards zero for larger k. These m are particularly distinctive. On the other hand, the phase shifts at $m = 2, 3, 4$, are very small in the range of ka that was accessible.

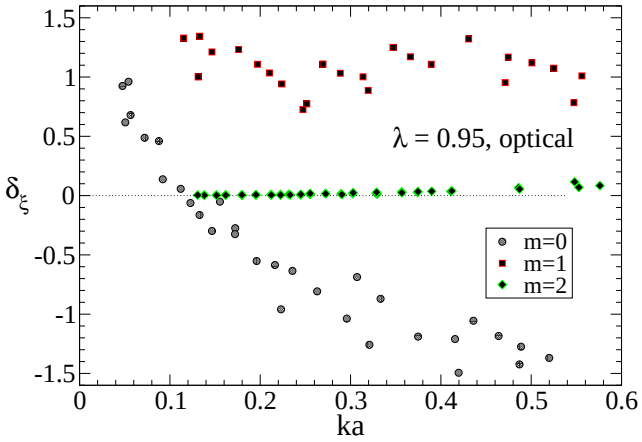

FIG. 21: (Color online) Optical mode scattering phase shifts versus wavevector for $\lambda = 0.95$, at the indicated angular momentum values m.

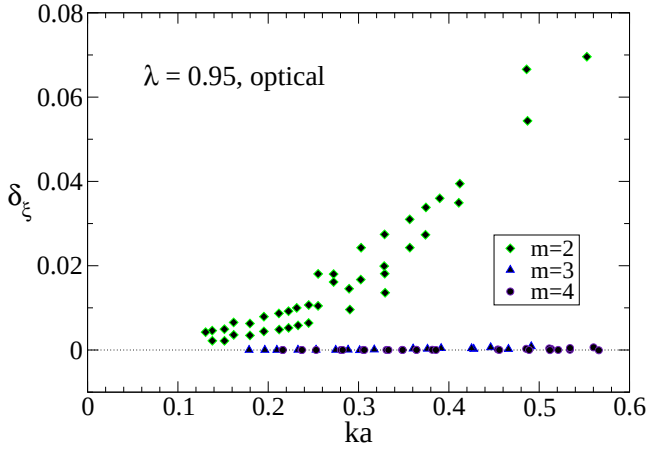

FIG. 22: (Color online) Optical mode scattering phase shifts versus wavevector for $\lambda = 0.95$, at the indicated angular momentum values m.

For comparison, the corresponding optical mode phase shifts at $\lambda = 0.95$ are shown in Figs. 21 and 22. The results are very similar to those at $\lambda = 0.954$, including the zero-crossing of the $m = 0$ shift near $ka \approx 0.12$. This is in contrast to the drastically different $\pi/2$ crossing points in the $m = 0$ acoustic phase shifts displayed above.

The simple analytical result for the optical modes obtained by using the continuum approach [see Eq. (16)] shows an overall qualitative and even quantitative agreement with the numerical calculations. For example, the case $m = 1$ with $r_0 = a$ leads to $\delta_{\xi(1)}(k) = \pi/2 + \arctan[J_1(ka)/N_1(ka)]$, which is in good quantitative agreement with the numerical results presented in Fig. 19. Indeed, the term $\arctan[J_1(ka)/N_1(ka)]$ is small and negative in the range in which ka is accessible, making $\delta_{\xi(1)}(k)$ decrease slowly from $\pi/2$ as ka increases. However, our simple continuum theory does not present the same success for the cases $m \geq 2$. In these cases, there is only a qualitative agreement with the numerical calculations. Actually, the analytical phase-shifts for $m > 1$ are also much smaller than that of the case $m = 1$, but they are relatively much larger than the numerical ones shown in Figs. 19 and 20. In these figures one can see clearly that, for $m > 1$, $\delta_{\xi(m)}(k) \to 0$ as $k \to 0$, while the analytical calculations imply to $\delta_{\xi(m)}(k) \to (\mid m \mid -\nu)\pi/2$ as $k \to 0$. Hence, numerical and analytical calculations differ essentially by a constant term, which tends to zero only for $m \gg 1$. We notice, therefore, that the causes of this quantitative disagreement for relatively large values of m must not be due to the boundary conditions used at the hole border. In fact, in these cases, the centrifugal barrier given by the term $-m^2/x^2$ in the scattering equation (5) becomes large, expelling the magnons from the center of the vortex and consequently from the border of the hole. Then the influence of the vacancy on the magnon phase-shifts should decrease as the angular momentum m grows. It is really confirmed by both the analytical and numerical calculations presented here.

V. VORTEX INSTABILITY LOCAL MODE

The VIM for vortices in a pure lattice (no vacancy) has a nearly circular symmetry, and is dominated by the out-of-plane fluctuations, corresponding to the field of the optical spin waves, ξ. It means that the angular quantum number $m = 0$ for this mode; for this reason it is not governed by the usual Bessel's equation, see Eq. (6) above. One can expect the same symmetry ($m = 0$) to apply for a vortex pinned on a vacancy or a circularly symmetric hole in the system. Furthermore, the η fluctuations can be ignored for analysis of the AFM VIM. The other essential physical feature of the VIM is the exponential decay with radius. This mode is localized on the vortex and its frequency falls within the gap of the optical spin wave branch, although it can be considered to be a state removed from that branch. It is a bound state of the effective potential $V(r)$, Eq. (3), and has no nodes, being the ground state of the Schrodinger problem (2a).

Using $m = 0$ in Eq. (5), and under the assumption of a bound state, $\omega < \omega_0$, the VIM field is seen to satisfy a modified Bessel's equation of imaginary order,

$$\xi^{''} + \frac{1}{x}\xi^{'} - \xi + \frac{q^2}{x^2}\xi = 0, \tag{41}$$

where now $x = \alpha r$, with a pure imaginary wavevector $k = i\alpha$, and real $\alpha = \sqrt{\frac{\Delta}{a^2} - (\frac{\omega}{c})^2}$. The order of the associated modified Bessel functions is $\nu = \pm iq$. The natural length scale in the problem is the radius of the hole. We seek an eigenfunction satisfying the boundary conditions $\xi(r_0) \neq 0$, $\xi(\infty) \to 0$. This can be accomplished in various ways. For example, we initially tried a variational approach, where the solution to Eq. (41) far from the origin is exponentially decaying like the function $\xi(r) = \xi_0 \exp(-\alpha r)$. Close to the origin, however, the wavefunction will be modified from this, due to the presence of the hole and its pinned vortex. The variational calculation works well and shows the basic important properties of the VIM. It can give only an overestimate of the VIM frequency, however, because the trial wavefunction is accurate only far from the vortex core. Since it over-estimates $E = (\omega/c)^2$, it must underestimate the critical anisotropy values.

We get better estimates of desired quantities by a numerical solution of the ordinary differential equation (ODE) (41), using a standard shooting method. To do so, it is more convenient to write it using the physical coordinates, as the radial Schrodinger equation

$$\frac{d^2\xi}{dr^2} + \frac{1}{r}\frac{d\xi}{dr} + [E - V(r)]\xi = 0. \tag{42}$$

Importantly, the ODE is integrated towards larger r, starting from a nonzero value $\xi(r_0) = \xi_0$ at the edge of the hole, with a small (or zero) initial slope. At the same time, the ODE is integrated towards smaller r, starting from some large radius R (the system outer cutoff), with fixed initial value $\xi(R) = 0$, and a small nonzero negative slope. The integration was effected by converting the problem to coupled first order ODEs and applying fourth-order Runge-Kutta integration with a fixed step size. The eigenvalue $E = (\omega/c)^2$ was adjusted together with the initial slopes iteratively until the two solutions and their first derivatives match at some intermediate point, which we took to be the classical turning point. Once convergence is achieved, the solution is exact to the numerical precision used. We used a grid along r of 20000 points, with $R = 100a$, for a hole radius $r_0 \leq 4a$.

For **vortex charge** $|\mathbf{q}| = \mathbf{1}$, typical normalized wavefunctions are shown in Fig. 23. The wavefunctions do not depend on the value of anisotropy Δ, which effects only a linear shift in the eigenenergy. One can note that the length scale of the wavefunction is truly determined by r_0; the wavefunction spreads in proportion to the hole radius. The curves shown will overlap if plotted as

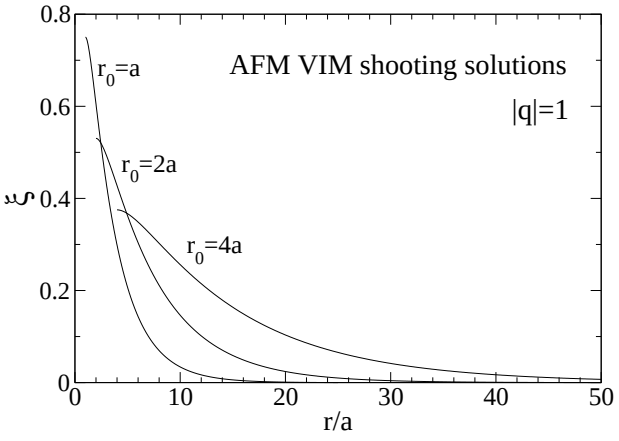

FIG. 23: Typical bound state radial wavefunctions of the AFM VIM for singly-charged vortices, for the indicated hole radii, obtained from numerical shooting of Eq. (42).

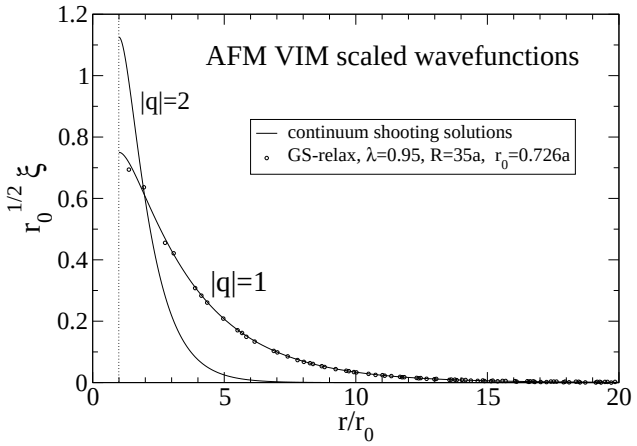

FIG. 24: Comparison of the bound state scaled radial wavefunctions of the AFM VIM, for singly and doubly charged vortices, obtained from numerical shooting of Eq. (42) (solid curves) and from GS relaxation solution on a square lattice, scaled using $r_0 = 0.726a$.

$r_0^{1/2}\xi(r/r_0)$. Due to this scaling, and consistently with the variational approach, the energy E is proportional to Δ/a^2 and falls to zero at the critical anisotropy. The numerical result obtained is

$$E = (\omega/c)^2 = \frac{\Delta}{a^2} - \frac{0.10226}{r_0^2}. \tag{43}$$

The last term is the squared inverse length parameter α^2, hence, the actual length scale of the wavefunctions is $\alpha^{-1} \approx 3r_0$. The anisotropy where the frequency goes to zero determines the critical anisotropy, below which a planar vortex develops nonzero out-of-plane components. The critical exchange and single ion anisotropy values result from the generalized anisotropy according to $\epsilon_c = \frac{1}{4}\Delta_c$ and $d_c = \frac{1}{2}\Delta_c$. The results can be summarized,

$$\Delta_c \approx 0.10226\frac{a^2}{r_0^2}, \quad d_c \approx 0.0511\frac{a^2}{r_0^2}, \quad \epsilon_c \approx 0.0256\frac{a^2}{r_0^2}. \tag{44}$$

The normalized wavefunctions for **vortex charge $|\mathbf{q}| = \mathbf{2}$** are compared to those for $|\mathbf{q}| = \mathbf{1}$ in Fig. 24, with both shown in scaled form. The deeper potential for $|q| = 2$ produces a wavefunction more tightly localized on the vortex. The numerical result for the energy is found to be

$$E = (\omega/c)^2 = \frac{\Delta}{a^2} - \frac{1.137}{r_0^2}. \tag{45}$$

In this case, the wavefunction length scale is $\alpha^{-1} \approx r_0$. The resulting estimates of the critical anisotropies are:

$$\Delta_c \approx 1.137\frac{a^2}{r_0^2}, \quad d_c \approx 0.568\frac{a^2}{r_0^2}, \quad \epsilon_c \approx 0.284\frac{a^2}{r_0^2}. \tag{46}$$

As for the case $|q| = 1$, the shooting solution is more accurate than the variational approach, because it accounts for the wavefunction better near the core region of the vortex.

It is clear that the above shooting results can be interpreted alternatively in terms a minimum (or critical) hole size r_c, necessary to stabilize the vortex in the planar form. The VIM frequencies can be expressed in the form,

$$\left(\frac{\omega a}{c}\right)^2 = \Delta\left(1 - \frac{r_c^2}{r_0^2}\right), \tag{47}$$

which implicitly defines the critical hole radii. For example, using the shooting solutions for $q = 1$ we have $r_c = a\sqrt{0.10226/\Delta}$, and for $q = 2$, $r_c = a\sqrt{1.137/\Delta}$. The result shows clearly how a larger hole is needed to stabilize planar vortices if the anisotropy is weak. If the hole radius is smaller than r_c, the vortex will change into an out-of-plane configuration. Furthermore, multiply-charged planar vortices require an even larger hole radius to be stabilized.

VI. DISCUSSION AND CONCLUSIONS: PHYSICAL EFFECTS OF A SPIN VACANCY OR HOLE

In this article, we have considered the problem of the interactions of magnons with pinned planar vortices in doped quasi-two-dimensional classical magnetic materials. Both analytical and numerical calculations were applied. Our calculations indicate that strong antiferromagnetic fluctuations around the vacancies have important effects in the scattering process. They affect the phase-shifts and also the vortex internal mode considerably. These results may have also some relevance to the counterpart 2D quantum spin systems. Indeed, recent nuclear-magnetic-resonance measurements have shown that when a Cu^{2+} in the $Cu-O$ plane of the cuprates

is substituted by a strong nonmagnetic impurity, such as Zn^{2+}, the antiferromagnetic correlations are enhanced, not destroyed, around impurities[13,14]. Below we discuss and summarize the main results obtained here.

A. The Scattering States

In real antiferromagnetic systems it is expected that, besides isolated impurities, there will be also clustering of nonmagnetic impurities. Our results can also be applied to this situation, where vortices could be, in principle, pinned on two or more nearest neighbor nonmagnetic impurities. In this case, the size of the hole (r_0) would be related to the number of nearest-neighbor impurities. The calculations presented here show that r_0 has a strong influence on the scattering process, changing the phase-shifts considerably. For holes larger than a, the change in the scattering of the out-of-plane magnons comes from the first term of Eq. 16 (the coupled vortex-hole contributions for the phase-shifts). The second term of Eq. 16 (the vortex contribution) is not modified as r_0 is varied. The change in the in-plane magnons comes only from the hole contribution (it seems that planar vortices do not affect the acoustic waves). However, the scattering problem considering next-nearest-neighbor impurities needs a more detailed analysis when a vortex is present. Indeed, the system will have at least two centers of scattering (probably, having an elliptical symmetry, instead of a circular one). Besides, the presence of a vortex may induce an effective interaction between vacancies, which is attractive[17], leading to stronger spin fluctuations in the region between the impurities. Certainly, it also affects the scattering of magnons.

For only one vacancy, we notice that our analytical calculations for the scattering interactions between magnons and the vortex pinned on a hole work relatively well for optical and acoustic modes only for $\mid m \mid > 0$. However, our continuum approximation fails completely for s-waves and, in our analysis, the reason is simple: in experimental situations involving small scales (as a small hole with size of the order of the lattice constant a) the application of the continuum theory, which is a long wavelength theory, should be viewed with caution, mainly when spin motion is taken into consideration. Here, without a centrifugal barrier, s-waves ($m = 0$) are able to strongly hit the vortex core and hence the border of the hole. It should imply that, for $m = 0$, the spin fluctuations in the small region around the hole become extremely complicated to be described by a long wavelength theory. Of course, it is already expected that strong discrete lattice effects not well described by the usual continuum approximation always appear from the core of the in-plane vortices.

B. The Local Mode

For a $q = 1$ vortex on a square lattice system without a hole, the critical anisotropies are known to be $d_c = 0.4690$ and $\epsilon_c = 0.2966$. These apply to a vortex centered in a plaquette–which can roughly be thought of as a hole with a radius less than one lattice constant. We can note here that the present calculations can reproduce these critical values approximately, if we take a hole size on the order of $r_0 \sim 0.3a$, although it is impossible to match both simultaneously since the discrete critical values are not in a 2 to 1 ratio.

A better comparison with the discrete lattice results can be obtained for a vortex centered on a single spin vacancy in the square lattice. There, the critical values are known to be $d_c = 0.0824$ and $\epsilon_c = 0.0455$, reduced considerably by the presence of the vacancy, consistent with these continuum predictions. For a single spin vacancy, there is the question: What hole size should be used in the corresponding continuum theory, to model a single vacancy? A choice of $r_0 = a$ is probably too large, if we consider that each lattice site has some effective half-width on the order of $a/2$. We can suppose that the hole radius should be slightly less than a, and try to choose it so that the continuum results roughly match the discrete results. Indeed, using $r_0 = \frac{3}{4}a$ in (44) gives $d_c = 0.091$ and $\epsilon_c = 0.0454$, both reasonably close to the discrete values.

Clearly, in a physical system where a larger set of spins is removed to form a larger circular spin hole, the continuum approach should be more precise, and Eqs. (44) will be more reliable. Then, these results indicate that vortices can be readily stabilized in the planar form, using very weak easy-plane anisotropy, if they can be formed around a large enough hole [radius greater than critical radius r_c, Eq. (47)] cut out of the spin system or material. The planar stability increases effectively with the area of the hole. Only in the limit $r_0 \to \infty$ do the critical anisotropy values fall to zero, which would destabilize any planar vortex.

C. Pinned Doubly Charged Vortices

Numerical stability calculations for doubly-charged vortices pinned on a single spin vacancy in a square lattice indicated the critical exchange anisotropy $\epsilon_c \approx 0.46$ (or $\lambda_c \approx 0.54$). These vortices also have only a narrow range of weaker anisotropy where they remain as stable *out-of-plane* vortices – without adequate anisotropy, a $q = 2$ vortex splits into a pair of $q = 1$ vortices. Assuming that the vacancy is modeled by a hole size on the order of $r_0 = \frac{3}{4}a$, as used above, our shooting solution for the continuum limit [Eq. (46)] produces $\epsilon_c \approx 0.51$. Considering that the $q = 2$ vortex spin field within 1 – 2 lattice constants of the core cannot be very well approximated by a continuum field, the agreement between these is remarkable. Most significantly, this calculation

shows that the instability of planar pinned $q = 2$ vortices to develop out-of-plane components is related to a localized dynamic oscillation mode of the vortex, analogous to that for pinned or unpinned $q = 1$ vortices.

One can also try to understand why stable doubly-charged vortices never occur in the pure square lattice (no vacancies) system with exchange anisotropy, using the present theory. This cannot simply be due to their higher energy (proportional to q^2) compared to singly-charged vortices. We can suppose a $q = 2$ vortex centered in a plaquette, considered as a hole of size $r_0 \approx 0.3a$, as used for the $q = 1$ stability question, which is also the same order as the cutoff needed to fit the continuum vortex energy to the discrete lattice energy. Then the shooting solution equations (46) predict critical exchange anisotropy $\epsilon_c \approx 3$, or $\lambda_c \approx -2$. This is significantly outside the realm of anisotropy constant valid for the easy-plane model; typically values of ϵ greater than 1 (XY model) are not considered, because they would imply exchange couplings of the opposite sign for the out-of-plane spin components. Stated otherwise, the exchange anisotropy required to stabilize a planar $q = 2$ vortex is not achievable in the usual easy-plane Heisenberg model.

In conclusion, the above results indicate that planar vortices with $q = 1$ or $q = 2$ may be found even in nearly isotropic diluted magnetic compounds. Possible candidates can be the layered structures $(R - NH_3)_2 M_y Mn_{1-y} X_4$, where R is an organic radical separating the MnX planes and the X ligand is either Cl or Br. The spin of Mn ion ($S = 5/2$) ensures that these compounds are well approximated by a classical Hamiltonian, and the nonmagnetic doping ions M can be Mg or Cd.

APPENDIX A: LEAST SQUARES WAVEFUNCTION FITS

A general wavefunction ψ (either η or ξ) is fitted to the expression with fitting parameters a_1, a_2, b_1, b_2,

$$\begin{aligned}\psi_{\rm fit}(r,\varphi) &= [a_1 J_\nu(kr) + b_1 N_\nu(kr)]\, e^{im\varphi} \\ &+ [a_2 J_\nu(kr) + b_2 N_\nu(kr)]\, e^{-im\varphi}. \quad \text{(A1)}\end{aligned}$$

For acoustic modes, the order is $\nu = m$, whereas for optical modes, $\nu = \sqrt{m^2 - q^2}$. When $m = 0$, we can set $a_2 = b_2 = 0$ and define a function with only two fitting parameters. From actual wavefunction data points, ψ_n, where n refers to lattice sites, the parameters need to be chosen to minimize the sum of squared deviations,

$$\chi = \sum_n |\psi_n - \psi_{\rm fit}(r_n, \varphi_n)|^2. \quad \text{(A2)}$$

Taking partial derivatives with respect to the fitting parameters leads to a matrix problem,

$$MX = Y, \quad \text{(A3)}$$

where the matrix M is composed from a sum over terms on each site of the lattice,

$$M = \sum_n m_n, \quad \text{(A4)}$$

and each m_n is given by a matrix

$$\begin{bmatrix} J_\nu J_\nu^* & J_\nu J_\nu^* e^{-2im\varphi} & N_\nu J_\nu^* & N_\nu J_\nu^* e^{-2im\varphi} \\ J_\nu J_\nu^* e^{2im\varphi} & J_\nu J_\nu^* & N_\nu J_\nu^* e^{2im\varphi} & N_\nu J_\nu^* \\ J_\nu N_\nu^* & J_\nu N_\nu^* e^{-2im\varphi} & N_\nu N_\nu^* & N_\nu N_\nu^* e^{-2im\varphi} \\ J_\nu N_\nu^* e^{2im\varphi} & J_\nu N_\nu^* & N_\nu N_\nu^* e^{2im\varphi} & N_\nu N_\nu^* \end{bmatrix} \quad \text{(A5)}$$

It is understood that each Bessel function is evaluated at argument $x = kr_n$, and additionally, the angular arguments are the angular positions of the lattice sites, $\varphi = \varphi_n$. X is a column vector containing the unknown fitting parameters, and Y is a sum over lattice sites, using the given mode wavefunction:

$$X = \begin{pmatrix} a_1 \\ a_2 \\ b_1 \\ b_2 \end{pmatrix}, \quad Y = \sum_n \begin{pmatrix} \psi_n J_\nu^* e^{-im\varphi} \\ \psi_n J_\nu^* e^{im\varphi} \\ \psi_n N_\nu^* e^{-im\varphi} \\ \psi_n N_\nu^* e^{im\varphi} \end{pmatrix} \quad \text{(A6)}$$

The linear system (A3) is solved for X by Gauss-Jordan elimination, leading to the least-squares estimate of the fitting parameters. For acoustic modes and for optical modes with $m^2 > q^2$, ν is real and so are the Bessel functions. For the special case of optical modes with $m^2 < q^2$, ν becomes imaginary, as do the Bessel functions, a situation whose calculations are further elaborated in Appendix B.

APPENDIX B: BESSEL FUNCTIONS J_i AND N_i

For the fitting of the $m = 0$ optical mode wavefunctions on a $q = 1$ pinned vortex, the complex Bessel functions $J_i(x)$ and $N_i(x)$ are required. These are not commonly available in a standard C or FORTRAN subroutine. Instead, $J_i(x)$ was implemented using C-programming with complex arithmetic, of the series expansion,

$$J_i(x) = \left(\frac{x}{2}\right)^i \sum_{n=0}^{\infty} \left(\frac{-x^2}{4}\right)^n \frac{1}{n!\,\Gamma(n+i+1)}. \quad \text{(B1)}$$

The sum was arranged as $J_i(x) = \sum_{n=0}^{\infty} t_n$, where successive terms are obtained by an iteration:

$$t_n = \frac{-x^2}{4} \frac{t_{n-1}}{n(n+i)}, \quad t_0 = \left(\frac{x}{2}\right)^i \frac{1}{\Gamma(i+1)}. \quad \text{(B2)}$$

The value $\Gamma(i+1) = i\Gamma(i) \approx 0.498016 - i\ 0.15495$ (from Maple or Mathematica) is used to initiate the series. The iteration is terminated when the sum for J_i converges to machine double precision. Typically, less than 30 terms are needed as long as argument x is less than 10, which is almost always the case for these low frequency modes

on small lattices (i.e., $x_{\max} = k \times R \approx 0.1 \times 40 = 4$). The Neumann function at this order is subsequently obtained from the standard relation between J_ν and N_ν,

$$N_i(x) = \frac{J_i(x)\cos i\pi - J_{-i}(x)}{\sin i\pi}, \qquad \text{(B3)}$$

where additionally, the relation $J_{-i}(x) = J_i^*(x)$ holds.

ACKNOWLEDGMENTS

GMW is very grateful for support from FAPEMIG as a visiting researcher and for the hospitality of Universidade Federal de Viçosa and of Universidade Federal de Santa Catarina, Brazil. ARP thanks CNPq and CAPES for financial support.

* Electronic address: apereira@ufv.br

† Electronic address: wysin@phys.ksu.edu; URL: `http://www.phys.ksu.edu/personal/wysin`

[1] B.V. Costa, M.E. Gouvêa, and A.S.T. Pires, Phys. Lett. A **165**, 179 (1992).

[2] A.R. Pereira, A.S.T. Pires, and M.E. Gouvêa, Solid. St. Comm. **86**, 187 (1993).

[3] A.R. Pereira, F.O. Coelho, and A.S.T. Pires, Phys. Rev. B **54**, 6084 (1996); M.P.P. Fonseca and A.S.T. Pires, Phys. Rev. B **73**, 012403 (2006).

[4] G.M. Wysin and A.R. Völkel, Phys. Rev. B **52**,7412 (1995).

[5] B.A. Ivanov, A.K. Kolezhuk, and G.M. Wysin, Phys. Rev. Lett. **76**,511 (1996).

[6] G.M. Wysin and A.R. Völkel, Phys. Rev. B **54**,12921 (1996).

[7] B.A. Ivanov, H.J. Schnitzer, F.G. Mertens, and G.M. Wysin, Phys. Rev. B **58**,8464 (1998).

[8] B.A. Ivanov and G.M. Wysin, Phys. Rev. B **65**, 134434 (2002).

[9] D.D. Sheka, I.A. Yastremsky, B.A. Ivanov, G.M. Wysin, and F.G. Mertens, Phys. Rev. B **69**, 054429 (2004).

[10] D.P. Landau, K.K. Mon, and H.-B. Schötler, eds., *Computer Simulation Studies in Condensed Matter Physics-Classical spin dynamics in the two-dimensional anisotropic Heisenberg model* (Spriger-Verlag, Berlim, 1988).

[11] G.M. Wysin, Phys. Rev. B **49**, 8780 (1994).

[12] F.G. Mertens, H.J. Schnitzer, and A.R. Bishop, Phys. Rev. B **56**, 2510 (1997).

[13] M.-H. Julien, T. Fehér, M. Horvatić, C. Berthier, O.N. Bakharev, P. Ségransan, G. Collin, and J.-F. Marucco, Phys. Rev. Lett. **84**, 3422 (2000).

[14] J. Bobroff, H. Alloul, W.A. MacFarlane, P. Mendels, N. Blanchard, G. Collin, and J.-F. Marucco, Phys. Rev. Lett. **86**, 4116 (2001).

[15] L.A.S. Mól, A.R. Pereira, and W.A. Moura-Melo, Phys. Rev. B **67**, 132403 (2003).

[16] A.R. Pereira, J. Appl. Phys. **97**, 094303 (2005); Phys. Rev. B **71**, 224404 (2005).

[17] F.M. Paula, A.R. Pereira, L.A.S.Mól, Phys. Lett.A **329**, 155 (2004).

[18] A.R. Pereira, Phys. Lett. A **314**, 102 (2003).

[19] A.R. Pereira, L.A.S. Mól, S.A. Leonel, P.Z. Coura, and B.V. Costa, Phys. Rev. B **68**, 132409 (2003).

[20] A.R. Pereira, S.A. Leonel, P.Z. Coura, and B.V. Costa, Phys. Rev.B **71**, 014403 (2005).

[21] M. Rahm, J. Biberger, V. Umansky, and D. Weiss, J. Appl. Phys. **93**, 7429 (2003).

[22] M. Rahm, R. Höllinger, V. Umansky, and D. Weiss, J. Appl. Phys. **95**, 6708 (2004).

[23] G.M. Wysin, Phys. Rev. B **68**, 184411 (2003).

[24] S.A. Leonel, P.Z. Coura, A.R. Pereira, L.A.S. Mól, and B.V. Costa, Phys. Rev. B **67**, 104426 (2003).

[25] B. Berche, A.I. Farinas-Sanches, Y. Holovatch, and R. Paredes, Eur. Phys. J. B **36**, 91 (2003).

[26] G.M. Wysin, Phys. Rev. B **71**, 094423 (2005).

[27] G.M. Wysin, A.R. Pereira, I.A. Marques, S.A. Leonel, and P.Z. Coura, Phys. Rev. B **72**, 094418 (2005).

[28] V.L. Berezinskii, Sov. Phys. JEPT **32**, 493 (1970).

[29] V.L. Berezinskii, Sov. Phys. JEPT **34**, 610 (1972).

[30] J.M. Kosterlitz and D.J. Thouless, J. Phys. C **6**, 1181 (1973).

[31] C.E. Zaspel, J.E. Drumheller, and K. Subbaraman, Phys. Stat. Sol. (a) **189**, 1029 (2002).

[32] K. Subbaraman, C.E. Zaspel, and J.E. Drumheller, Phys. Rev. Lett. **80**, 2201 (1998).

[33] F.M. Paula, A.R. Pereira, and G.M. Wysin, Phys. Rev. B **72**, 094425 (2005).

[34] C.E. Zaspel, C.M. McKennan, and S.R. Snaric, Phys. Rev. B **53**, 11317 (1996).

[35] G.M. Wysin, M.E. Gouvêa, and A.S.T. Pires, Phys. Rev. B **57**, 8274 (1998).

[36] G.M. Wysin, Phys. Rev. B **63**, 094402 (2001).

[37] On a square lattice, due to discreteness effects, m is a good quantum number only when it is odd, see Ref. 7; then the modes at $\pm m$ are exactly degenerate. There are no exact eigenstates at even m; a mixture of $+m$ and $-m$ states is required. Then the even values of m give a pair of states with a small splitting. Ignoring this effect, we identify the modes here simply by positive values of m.